

Learning Quantum Data Distribution via Chaotic Quantum Diffusion Model

Quoc Hoan Tran,^{*} Koki Chinzei, Yasuhiro Endo, and Hiroataka Oshima

Quantum Laboratory, Fujitsu Research, Fujitsu Limited, Kawasaki, Kanagawa 211-8588, Japan

(Dated: February 26, 2026)

Generative models for quantum data pose significant challenges but hold immense potential in fields such as chemoinformatics and quantum physics. Quantum denoising diffusion probabilistic models (QuDDPMs) enable efficient learning of quantum data distributions by progressively scrambling and denoising quantum states; however, existing implementations typically rely on circuit-based random unitary dynamics that can be costly to realize and sensitive to control imperfections, particularly on analog quantum hardware. We propose the chaotic quantum diffusion model, a framework that generates projected ensembles via chaotic Hamiltonian time evolution, providing a flexible and hardware-compatible diffusion mechanism. Requiring only global, time-independent control, our approach substantially reduces implementation overhead across diverse analog quantum platforms while achieving accuracy comparable to QuDDPMs. This method improves trainability and robustness, broadening the applicability of quantum generative modeling.

INTRODUCTION

Generative models aim to synthesize diverse data by learning their underlying probability distributions and play a central role in data understanding, simulation, and discovery. Quantum circuits are capable of generating classically intractable probability distributions, motivating the use of quantum systems as generative models that may outperform their classical counterparts in certain regimes. Along this line, a variety of quantum generative models have been proposed for classical data generation, including quantum generative adversarial networks (QuGANs) [1–3], quantum variational autoencoders (QVAEs) [4, 5], tensor-network-based models [6], and diffusion-based quantum models [7, 8]. Despite these developments, a clear empirical advantage over classical generative models has yet to be established.

More recently, growing attention has shifted toward quantum machine learning (QML) for quantum data, where the data themselves originate from quantum systems [9]. Unlike classical data such as text or images, quantum data inherently encode quantum correlations, entanglement, and measurement statistics, posing fundamental challenges that cannot be addressed by classical generative models alone. Efficient generation of quantum data is essential for advancing our understanding of quantum many-body systems and for applications in chemistry, biology, and materials science. Since quantum data generation intrinsically relies on quantum resources, quantum-native generative models are a natural and necessary choice.

Existing quantum generative models such as QuGANs and QVAEs can be used to prepare individual target quantum states [10–12], but they are generally inefficient at learning and generating ensembles of quantum states [13]. This limitation arises primarily from the need to train deep variational quantum circuits (VQCs), which suffer from optimization challenges such as barren plateaus [14]. The quantum denoising diffusion proba-

bilistic model (QuDDPM) [15] addresses these issues by extending the classical diffusion paradigm to quantum data. QuDDPM learns a sequence of intermediate distributions that interpolate smoothly between a structured target distribution \mathcal{E}_0 and a maximally scrambled distribution, using quantum scrambling for the forward diffusion process and measurement-enabled VQCs for backward denoising. This layerwise training strategy improves trainability and mitigates barren plateaus. However, existing realizations of QuDDPM rely on circuit-based scrambling using random unitary circuits (RUCs), which require fine-grained spatio-temporal control and substantial circuit depth. These requirements pose significant challenges for implementation, particularly on analog quantum platforms where control is typically global and time-independent.

In this work, we propose a chaotic quantum diffusion model that replaces circuit-based scrambling with chaotic Hamiltonian time evolution. By generating projected ensembles through quantum chaos, our approach provides a flexible and hardware-compatible diffusion mechanism that eliminates the need for explicit RUCs, enabling efficient implementation across a broad range of quantum hardware.

QUANTUM DENOISING DIFFUSION PROBABILISTIC MODEL (QUDDPM)

We address the problem of learning quantum data distributions and explain the idea of the QuDDPM model in the literature [Fig. 1(a)]. Consider a training dataset \mathcal{S} of N independent quantum states drawn from an unknown probability distribution \mathcal{E}_0 . A generative model is characterized by a parameterized probability distribution \mathcal{E}_θ , from which samples can be drawn. If \mathcal{E}_θ is realized through VQCs, θ corresponds to the adjustable parameters of these circuits. The training goal is to obtain a distribution \mathcal{E}_θ that closely approximates \mathcal{E}_0 . We opti-

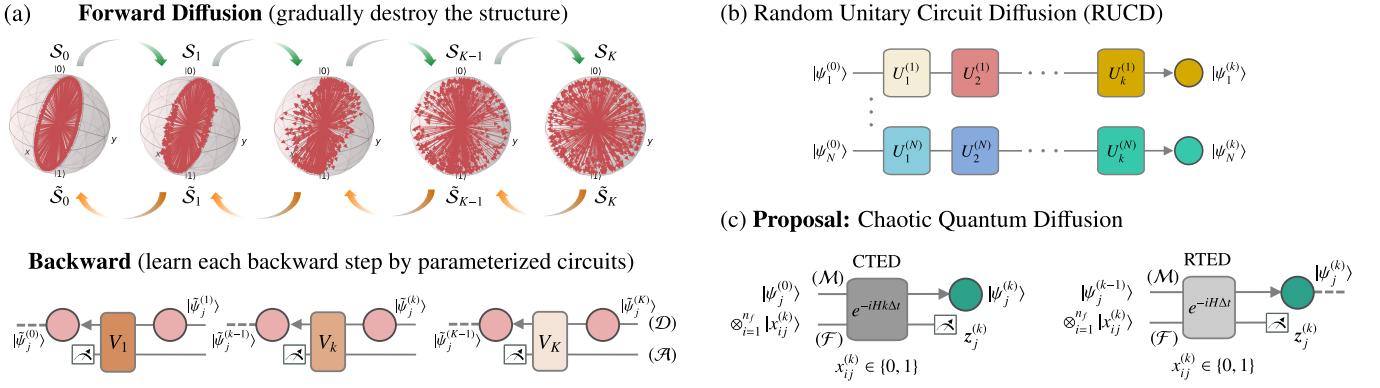


FIG. 1. (a) The general scheme of quantum denoising diffusion probabilistic model. (b) The implementation of the random unitary circuit diffusion (RUCD) model. (c) The chaotic quantum diffusion model in our proposal.

minimize the distance $D(\mathcal{E}_\theta, \mathcal{E}_0)$ such as the Maximum Mean Discrepancy (MMD) and Wasserstein distance between these distributions. Since $D(\mathcal{E}_\theta, \mathcal{E}_0)$ cannot be computed directly, we take a dataset \mathcal{S}_θ sampling from \mathcal{E}_θ and compute the distance $D(\mathcal{S}, \mathcal{S}_\theta)$. In the inference phase, we fix the trained θ and generate new states $|\psi\rangle \sim \mathcal{E}_\theta$.

Unlike prior quantum models that focus on generating average states such as fully mixed states, QuDDPM targets entire distributions of states, enabling the generation of correlated or structured quantum data. QuDDPM builds on the success of classical DDPMs in tasks such as image generation but extends them to quantum data. Classical DDPMs use Gaussian noise addition in a forward process to gradually corrupt data toward a noise distribution (e.g., an isotropic Gaussian), followed by learned denoising in the reverse process. QuDDPM replaces Gaussian noise with scrambling RUCs in the forward process, applying random unitaries that evolve quantum states toward a near-Haar-random distribution. This choice is more natural for quantum systems, as Gaussian noise does not directly correspond to physically valid unitary dynamics.

In the backward process, QuDDPM employs measurement-enabled denoising using VQCs with ancilla qubits and projective measurements. The ancilla qubits are entangled with the system qubits via controlled, parameterized operations, and subsequent measurements collapse the ancilla states, effectively denoising by projecting the system onto subspaces that approximate the target distribution. These measurement-induced, non-unitary operations are essential for breaking the constraints of purely unitary quantum circuits and enabling flexible generative modeling. This contrasts with fully unitary quantum models, which are limited in expressivity when learning inherently non-unitary processes such as noise.

Forward diffusion process

In the forward diffusion process using RUCs, K random unitary gates $U_1^{(j)}, \dots, U_K^{(j)}$ are applied to each sample $|\psi_j^{(0)}\rangle$ ($j = 1, \dots, N$) in the training dataset \mathcal{S} [Fig. 1(b)]. This evolves the ensemble $\mathcal{S}_k = \left\{ |\psi_j^{(k)}\rangle = \prod_{l=1}^k U_l^{(j)} |\psi_j^{(0)}\rangle \right\}_j$ toward a Haar-random states ensemble over the Hilbert space. We define this scheme as RUCs diffusion (RUCD). Assuming the execution time for each $U_k^{(j)}$ is τ_u , the execution time to generate each \mathcal{S}_k is $\tau_u N k$. Therefore, the RUCD requires NK random unitary gates with $\tau_u N \sum_{k=1}^K k = \tau_u N K(K+1)/2$ execution time to generate all \mathcal{S}_k .

The forward diffusion process does not require exact Haar randomness. Recent studies have shown that shallow random circuits can efficiently approximate unitary k -designs with depth scaling polynomially or even logarithmically in system size for small k [16]. Such approximate designs are sufficient to induce rapid scrambling of local observables and correlations, making them suitable for diffusion-based generative modeling. QuDDPM's implementation relies on approximate scrambling rather than high-fidelity Haar sampling. Nevertheless, even shallow circuit constructions for approximate designs require explicit gate-level control and circuit compilation, which can be costly or infeasible on analog quantum platforms. This motivates alternative diffusion mechanisms that naturally generate effective scrambling without the need for circuit-based random unitaries.

Backward denoising process

The backward process starts with an ensemble $\tilde{\mathcal{S}}_K = \{|\tilde{\psi}_j^{(K)}\rangle\}_j$ sampled from Haar-random states and reduces noise step by step. In practice, since it is difficult to sample from a complete Haar-random state distribution, $\tilde{\mathcal{S}}_K = \{|\tilde{\psi}_j^{(K)}\rangle\}_j$ are sampled from the prod-

uct of single-qubit Haar-random states. As depicted in Fig. 1(a), the denoising step applies a parameterized unitary $V_k = V(\boldsymbol{\theta}_k)$ to the data system \mathcal{D} (input $|\tilde{\psi}_j^{(k)}\rangle$) and n_a ancilla qubits in the ancilla system \mathcal{A} ($|\mathbf{0}\rangle_{\mathcal{A}}$), followed by projective measurements in the computational basis on \mathcal{A} , yielding the state $|\tilde{\psi}_j^{(k-1)}\rangle$ in \mathcal{D} . Assuming the measurement outcome $\mathbf{z}_j^{(k)}$ is obtained on the ancilla, this operation is formulated as

$$\begin{aligned} \Phi_j^{(k)}(|\tilde{\psi}_j^{(k)}\rangle) &= \frac{(\mathbb{I}_{\mathcal{D}} \otimes \Pi_{\mathcal{A}})V_k |\tilde{\Psi}_j^{(k)}\rangle}{\sqrt{\langle \tilde{\Psi}_j^{(k)} | V_k^\dagger (\mathbb{I}_{\mathcal{D}} \otimes \Pi_{\mathcal{A}}) V_k | \tilde{\Psi}_j^{(k)} \rangle}} \quad (1) \\ &= |\tilde{\psi}_j^{(k-1)}\rangle \otimes |\mathbf{z}_j^{(k)}\rangle_{\mathcal{A}}, \quad (2) \end{aligned}$$

where $\Pi_{\mathcal{A}} = |\mathbf{z}_j^{(k)}\rangle \langle \mathbf{z}_j^{(k)}|_{\mathcal{A}}$ and $|\tilde{\Psi}_j^{(k)}\rangle = |\tilde{\psi}_j^{(k)}\rangle \otimes |\mathbf{0}\rangle_{\mathcal{A}}$.

Training involves K cycles with a layerwise scheme. At the cycle $(K - k + 1)$ (with $k = K, \dots, 1$), the forward diffusion with $U_1^{(j)}$ to $U_{k-1}^{(j)}$ generates the noisy ensemble $\mathcal{S}_{k-1} = \{|\psi_j^{(k-1)}\rangle\}_j$. Parameters of $V(\boldsymbol{\theta}_k)$ are optimized to make the denoised ensemble $\tilde{\mathcal{S}}_{k-1} = \{|\tilde{\psi}_j^{(k-1)}\rangle\}_j$ approximate \mathcal{S}_{k-1} via the minimization of the cost function $D(\mathcal{S}_{k-1}, \tilde{\mathcal{S}}_{k-1})$. After optimization, the parameters $\boldsymbol{\theta}_k$ are fixed for use in the next cycle to optimize $\boldsymbol{\theta}_{k-1}$. This layerwise training approach divides the original training problem into K manageable sub-tasks, ensuring convergence for incremental distribution transitions and mitigating issues such as barren plateaus [14].

The cost function in QuDDPM measures the similarity between two quantum state ensembles using a symmetric, positive definite quadratic kernel $\kappa(|\mu\rangle, |\phi\rangle)$. This kernel can be defined by the state fidelity computed via the SWAP test (Fig. 2) or directly derived from the classical shadows kernel [17, 18]. We consider two cost functions D_{MMD} and D_{Wass} , corresponding to MMD distance and 1-Wasserstein distance based on the state fidelity.

The MMD distance between two state ensembles $\mathcal{X} = \{|\mu_i\rangle\}$ and $\mathcal{Y} = \{|\psi_j\rangle\}$ is defined as

$$D_{\text{MMD}}(\mathcal{X}, \mathcal{Y}) = \bar{\kappa}(\mathcal{X}, \mathcal{X}) + \bar{\kappa}(\mathcal{Y}, \mathcal{Y}) - 2\bar{\kappa}(\mathcal{X}, \mathcal{Y}), \quad (3)$$

where $\bar{\kappa}(\mathcal{X}, \mathcal{Y}) = \mathbb{E}_{|\mu\rangle \in \mathcal{X}, |\phi\rangle \in \mathcal{Y}}[\kappa(|\mu\rangle, |\phi\rangle)]$.

The 1-Wasserstein distance is further presented as an enhancement in the situation where the MMD distance is not feasible to distinguish two state ensembles. Given normalized κ (i.e., $\kappa(|\phi\rangle, |\phi\rangle) = 1 \forall |\phi\rangle$), the pairwise cost matrix $\mathbf{C} = (C_{i,j}) \in \mathbb{R}^{|\mathcal{X}| \times |\mathcal{Y}|}$ is computed as $C_{i,j} = 1 - \kappa(|\mu_i\rangle, |\psi_j\rangle)$. The 1-Wasserstein distance is calculated via the formulation of the optimal transport problem into a linear programming procedure to find the optimal transport plan $\mathbf{P} = (P_{i,j}) \in \mathbb{R}^{|\mathcal{X}| \times |\mathcal{Y}|}$:

$$D_{\text{Wass}}(\mathcal{X}, \mathcal{Y}) = \min_{\mathbf{P}} \sum_{i,j} P_{i,j} C_{i,j}, \quad (4)$$

$$\text{s.t. } \mathbf{P}\mathbf{1}_{|\mathcal{Y}|} = \mathbf{a}, \quad \mathbf{P}^\top \mathbf{1}_{|\mathcal{X}|} = \mathbf{b}, \quad \mathbf{P} \geq 0. \quad (5)$$

Here, $\mathbf{1}_{|\mathcal{X}|}$ and $\mathbf{1}_{|\mathcal{Y}|}$ are all-ones vectors with size $|\mathcal{X}|$ and $|\mathcal{Y}|$, respectively, and $\mathbf{a} \in \mathbb{R}^{|\mathcal{X}|}$ and $\mathbf{b} \in \mathbb{R}^{|\mathcal{Y}|}$ are the probability vectors histogram corresponding to \mathcal{X} and \mathcal{Y} . Normally, we set uniform histograms as $\mathbf{a} = \frac{1}{|\mathcal{X}|} \mathbf{1}_{|\mathcal{X}|}$ and $\mathbf{b} = \frac{1}{|\mathcal{Y}|} \mathbf{1}_{|\mathcal{Y}|}$.

PROPOSAL: CHAOTIC QUANTUM DIFFUSION

RUCD demands significant computational overhead in designing sequences of random gates, rendering it unsuitable for many quantum systems, particularly analog platforms such as Rydberg atom arrays and ultracold atoms in optical lattices. These platforms excel in simulating continuous-time dynamics via global Hamiltonians but lack the fine-grained, time-dependent control needed for arbitrary gate sequences. Implementing RUCD on analog hardware would require digitizing the process through Trotterization or pulse shaping, which introduces approximation errors and increases susceptibility to noise from environmental couplings.

We address this challenge by adopting the projected ensemble framework [19–21], which utilizes a single chaotic many-body wave function to generate a random ensemble of pure states on a subsystem. In this framework, projective measurements are performed on the larger subsystem of a bipartite state undergoing quantum chaotic evolution. This process yields a set of pure states on the smaller subsystem, accompanied by their respective Born probabilities. Collectively, these states form the projected ensemble, which converges to a state design when the measured subsystem is sufficiently large. A chaotic Hamiltonian in this context is characterized by non-integrability, ergodic dynamics, spectral properties resembling those of random matrix theory, and strong entanglement generation. Recent works have further clarified the role of symmetry in the Hamiltonian and measurement structure in the emergence of state designs from projected ensembles [22].

Our approach offers significant advantages over RUCD, as it requires only global and time-independent control. Consequently, it is more accessible and adaptable to a wide range of quantum systems, including analog platforms, where precise gate sequences are challenging to implement.

Projected Ensemble

We consider a many-body system partitioned into a subsystem \mathcal{M} (with n_m qubits) and its complement \mathcal{F} (with n_f qubits). Given a generator state $|\Phi\rangle$ on the total system $\mathcal{M} + \mathcal{F}$, which is produced by chaotic evolution, we perform local measurements on \mathcal{F} , typically in the computational basis. This yields differ-

ent pure states $|\Phi_{\mathcal{M}}(\mathbf{z}_{\mathcal{F}})\rangle$ on \mathcal{M} , each corresponding to a distinct measurement outcome $\mathbf{z}_{\mathcal{F}}$, which are bit-strings of the form, for example, $\mathbf{z}_{\mathcal{F}} = 001\dots 010$. The collection of these states, together with probabilities $p(\mathbf{z}_{\mathcal{F}}) = \|(\mathbb{I}_{\mathcal{M}} \otimes \langle \mathbf{z}_{\mathcal{F}} |) |\Phi\rangle\|^2$, forms the projected ensemble on \mathcal{M} : $\{|\Phi_{\mathcal{M}}(\mathbf{z}_{\mathcal{F}})\rangle, p(\mathbf{z}_{\mathcal{F}})\}_{\mathbf{z}_{\mathcal{F}}}$. The projected ensemble provides a full description of the total system state as $|\Phi\rangle = \sum_{\mathbf{z}_{\mathcal{F}}} \sqrt{p(\mathbf{z}_{\mathcal{F}})} |\Phi_{\mathcal{M}}(\mathbf{z}_{\mathcal{F}})\rangle \otimes |\mathbf{z}_{\mathcal{F}}\rangle$. We note that the ensemble of pure states is not just a density matrix. The density matrix represents the average mixed state over the distribution, capturing first-order statistics such as expectation values of observables. Therefore, different ensembles can lead to the same density matrix. These ensembles can be distinguished through their higher moments of the observable expectation values.

The chaotic dynamics scramble quantum information, resulting in universal correlations and randomness within the subsystem. For a case of infinite-temperature thermalization, with sufficiently large $n_f = \Omega(kn_m)$ and the generator state $|\Phi\rangle$ obtained by quenched time evolution of chaotic Hamiltonians, the projected ensemble approximates k -design of Haar-random states [19, 20]. This convergence is quantified by the trace distance $\Delta^{(k)} = \frac{1}{2} \|\rho_E^{(k)} - \rho_{\text{Haar}}^{(k)}\|_1 \rightarrow 0$ for the k -th moment operators $\rho_E^{(k)}$ and $\rho_{\text{Haar}}^{(k)}$ calculated from the projected ensemble and the Haar-random states ensemble, respectively. Mathematically, this relies on the eigenstate thermalization hypothesis and the concentration of measure: the chaotic evolution scrambles quantum information universally, making higher moments converge to the Haar measure.

Inspired by this framework, we propose two schemes in which the diffusion is implemented through chaotic Hamiltonian evolution [Fig. 1(c)].

Cumulative Time Evolution Diffusion (CTED)

For each $|\psi_j^{(0)}\rangle \in \mathcal{S}_0$ on \mathcal{M} , we implement a diffusion process to obtain the k -step state $|\psi_j^{(k)}\rangle \in \mathcal{S}_k$. The initial state $|\mathbf{x}_j^{(k)}\rangle$ in \mathcal{F} is randomly sampled from the ensemble $\{|\mathbf{x}\rangle, q(\mathbf{x})\}_{\mathbf{x} \in \{0,1\}^{n_f}}$ of computational basis states with probability $q(\mathbf{x})$. Inspired from Ref. [21], we introduce $q(\mathbf{x})$ (uniform distribution in our experiments) here to increase classical randomness injected during the protocol, which is converted into quantum randomness of the resulting state ensemble. The input $|\psi_j^{(0)}\rangle \otimes |\mathbf{x}_j^{(k)}\rangle$ of the system $(\mathcal{M} + \mathcal{F})$ is then evolved cumulatively under the same unitary $e^{-iHk\Delta t}$ with $\forall j$, where H is a fixed chaotic Hamiltonian [20]. Subsequently, a random local measurement is performed on \mathcal{F} , yielding the measurement record $\mathbf{z}_j^{(k)}$ with the probability $p_{\mathbf{x}}(\mathbf{z}_j^{(k)}) = q(\mathbf{x}_j^{(k)}) \left\| \left(\mathbb{I}_{\mathcal{M}} \otimes \langle \mathbf{z}_j^{(k)} | \right) e^{-iHk\Delta t} \left(|\psi_j^{(0)}\rangle \otimes |\mathbf{x}_j^{(k)}\rangle \right) \right\|^2$, and

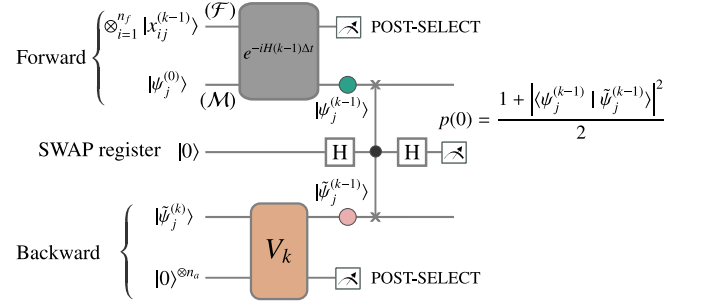


FIG. 2. The schematic circuit to compute the fidelity between the forward state $|\psi_j^{(k-1)}\rangle$ and the denoised state $|\tilde{\psi}_j^{(k-1)}\rangle$ using the SWAP test.

the resulting state $|\psi_j^{(k)}\rangle$ on \mathcal{M} . In this case, we obtain the *classically-enhanced* projected ensemble $\mathcal{E}^{(k)} = \{q(\mathbf{x}_j^{(k)})p_{\mathbf{x}}(\mathbf{z}_j^{(k)}); |\psi_{\mathbf{x}}(\mathbf{z}_j^{(k)})\rangle\}_j$.

Since the execution time for $e^{-iHk\Delta t}$ is generally considered scaling with k , we can assume the execution time for $e^{-iHk\Delta t}$ is $k\tau_c$. This CTED requires K unitaries and $\tau_c N \sum_{k=1}^K k = \tau_c N K(K+1)/2$ execution time to generate all \mathcal{S}_k .

In Fig. 2, we depict the schematic circuit to compute the state fidelity between the forward state $|\psi_j^{(k-1)}\rangle$ and the denoised state $|\tilde{\psi}_j^{(k-1)}\rangle$ can be computed using the SWAP test. The SWAP test consists of two Hadamard gates and a controlled-swap gate applied on $2n_m + 1$ qubits. The probability of measure 0 on the SWAP register is $p(0) = \frac{1}{2} + \frac{1}{2} \left| \langle \psi_j^{(k-1)} | \tilde{\psi}_j^{(k-1)} \rangle \right|^2$, which directly derives the fidelity. A post-selection protocol is applied to the projective measurements in the forward and backward processes, ensuring $|\psi_j^{(k-1)}\rangle$ and $|\tilde{\psi}_j^{(k-1)}\rangle$ remain consistent across SWAP test measurements.

Repeated Time Evolution Diffusion (RTED)

Unlike the CTED, we consider the input of $(\mathcal{M} + \mathcal{F})$ as $|\psi_j^{(k-1)}\rangle \otimes |\mathbf{x}_j^{(k)}\rangle$, where $|\psi_j^{(k-1)}\rangle \in \mathcal{S}_{k-1}$, then evolve this state under the unitary $e^{-iH\Delta t}$ with $\forall j$. This process is then repeated for $k = 1, \dots, K$. Assuming the execution time for $e^{-iH\Delta t}$ is τ_r , to generate each \mathcal{S}_k , we need to repeat $e^{-iH\Delta t}$ for k times, making the execution time is $k\tau_r$. Therefore, this RTED requires only one unitary but $\tau_r N \sum_{k=1}^K k = \tau_r N K(K+1)/2$ execution time to generate all \mathcal{S}_k .

Universal Ensemble

In the CTED and RTED schemes, the generator state at each diffusion step is generally not at infinite temperature. As a result, the forward diffusion operates in a

finite-temperature regime where convergence to the Haar measure is not expected [20]. In CTED, longer evolution times ($k\Delta t$) allow more scrambling. However, because the dynamics start from finite-energy states, the resulting projected ensembles remain constrained by energy conservation and saturate at a finite-temperature universal distribution. In RTED, resets on diffused states preserve some initial structure across steps, further deviating from full Haar scrambling. If the target distribution \mathcal{E}_0 were already Haar-random, the projected ensembles would converge to approximate k -designs, but in the general case, the target distributions are often low-entropy, making the finite-temperature-like distribution.

Recent work has shown that, under chaotic many-body dynamics at finite energy density, projected ensembles generically converge to Scrooge ensembles [23, 24]. These ensembles are universal in the sense that they reproduce ETH-predicted moments for local observables across different chaotic Hamiltonians, yet remain maximally constrained by conserved quantities such as energy [25]. From an information-theoretic perspective, Scrooge ensembles can be understood as maximum-entropy distributions subject to fixed macroscopic constraints, embodying the minimal amount of randomness required by the dynamics rather than full Haar randomness.

The Scrooge-like nature of the diffuse ensemble affects backward denoising but does not hinder trainability. In contrast to RUCD, where diffusion toward fully Haar-random states can lead to barren-plateau behavior in deep variational quantum circuits, the energy-dependent structure retained in finite-temperature diffusion may provide a smoother learning landscape. Our numerical results demonstrate that, despite deviating from Haar scrambling, CTED and RTED achieve generative accuracy comparable to RUCD while operating in a more physically realistic and information-efficient diffusion regime.

RESULTS

We conduct numerical experiments using three illustrative datasets: synthetic distributions of clustered quantum states, circular quantum states, and a quantum distribution derived from a chemistry dataset. We simulate the quantum circuits with the TensorCircuit library [26], and rely on JAX [27] for automatic differentiation to support gradient-based optimization. The circuit parameters are initialized uniformly within $[-\pi, \pi]$, and optimization is performed using the Adam algorithm with a learning rate of 0.001. Source code to reproduce these experiments is available in the GitHub repository [28].

For CTED and RTED, the dynamics are governed by a one-dimensional mixed-field Ising Hamiltonian with open boundary conditions, defined on the total system comprising $n_m + n_f$ sites as $H = \sum_{j=1}^{n_m+n_f} (h^x \sigma_j^x + h^y \sigma_j^y) +$

$J \sum_{j=1}^{n_m+n_f-1} \sigma_j^x \sigma_{j+1}^x$. Here, σ_j^μ (with $\mu = x, y, z$) denotes the Pauli operators at site j , J represents the interaction strength, and h^x and h^y are the strengths of the longitudinal and transverse magnetic fields, respectively. In the presence of a non-zero longitudinal field ($h^x \neq 0$), the Hamiltonian exhibits ergodic behavior [20], with its eigenvalues and eigenvectors conforming to the predictions of the ETH [29, 30]. To model the non-integrable regime, we adopt $h^x = 0.8090$, $h^y = 0.9045$, and $J = 1.0$. The time evolution is discretized with a time step of $\Delta t = 0.02$ over K diffusion steps.

For RUCD, we adopt the fast scrambling circuits from Ref. [15], applying $\prod_{l=1}^k U_k^{(j)}$ to each initial state $|\psi_j^{(0)}\rangle$. Here, $U_k^{(j)} = \Omega_k(s_k^{(j)})W_k(\mathbf{g}_k^{(j)})$, where $W_k(\mathbf{g}_k^{(j)})$ implements single-qubit rotations as $W_k(\mathbf{g}_k^{(j)}) = \bigotimes_{q=1}^{n_m} e^{-ig_{k,3q-1}^{(j)} \frac{Z_q}{2}} e^{-ig_{k,3q-2}^{(j)} \frac{Y_q}{2}} e^{-ig_{k,3q-3}^{(j)} \frac{Z_q}{2}}$, and an entangling layer $\Omega_k(s_k^{(j)})$ applies ZZ rotations across all qubit pairs as $\Omega_k(s_k^{(j)}) = \prod_{q_1 < q_2} \exp\left[\frac{-is_k^{(j)}}{2\sqrt{n_m}} Z_{q_1} Z_{q_2}\right]$. The ranges of uniformly random rotation angles $g_{k,q}^{(j)}$ and $s_k^{(j)}$ are tuned as $[-\alpha\pi/8, \alpha\pi/8]$ and $[0.4\alpha, 0.6\alpha]$, respectively. Here, α is the scaling parameter to control the diffusion speed, which is set as $\alpha = k^2/100$ at the k -th step.

In the backward process with n_a ancilla qubits, each V_k is constructed using a Hardware Efficient Ansatz on $n = n_m + n_a$ qubits with L layers as $V_k(\boldsymbol{\theta}_k) = \prod_{l=1}^L \tilde{\Omega}_k \tilde{W}_k(\boldsymbol{\theta}_k)$, where $\tilde{W}_k(\boldsymbol{\theta}_k) = \bigotimes_{q=1}^n e^{-i\theta_{k,2q-1} \frac{Y_q}{2}} e^{-i\theta_{k,2q-2} \frac{X_q}{2}}$ and $\tilde{\Omega}_k = \bigotimes_{q=1}^{\lfloor (n-1)/2 \rfloor} C Z_{2q,2q+1} \bigotimes_{q=1}^{\lfloor n/2 \rfloor} C Z_{2q-1,2q}$.

Learning Multi-cluster and Circular Distribution

We conduct numerical experiments to generate multi-cluster and circular ensembles of n_m -qubit quantum states ($n_m = 4$). The multi-cluster ensemble is a mixture of pure states centered around distinct clusters, modeling multimodal quantum data relevant to fields like quantum chemistry and quantum error correction. The target distribution is a mixture of three clusters: 40% from cluster 1, 40% from cluster 2, and 20% from cluster 3), each consisting of n_m -qubit pure states. Cluster 1 centers on $|0\rangle^{\otimes n_m}$, cluster 2 on $|1\rangle^{\otimes n_m}$, and cluster 3 on the GHZ state $\frac{1}{\sqrt{2}}(|0\rangle^{\otimes n_m} + |1\rangle^{\otimes n_m})$. To mimic imperfections in quantum hardware, we incorporated noise into each cluster by applying random single-qubit rotations, with rotation angles sampled from a Gaussian distribution $\mathcal{N}(0, \sigma^2)$ where $\sigma = 0.05$. For the circular ensemble, the quantum state has the form of $|\psi(\beta)\rangle = \cos(\beta/2) |0\dots 0\rangle + \sin(\beta/2) |1\dots 1\rangle$ of n_m qubits, where $\beta \in [0, 2\pi]$.

We investigate the evolved dynamics of the diffused ensembles derived from CTED and RTED. Given

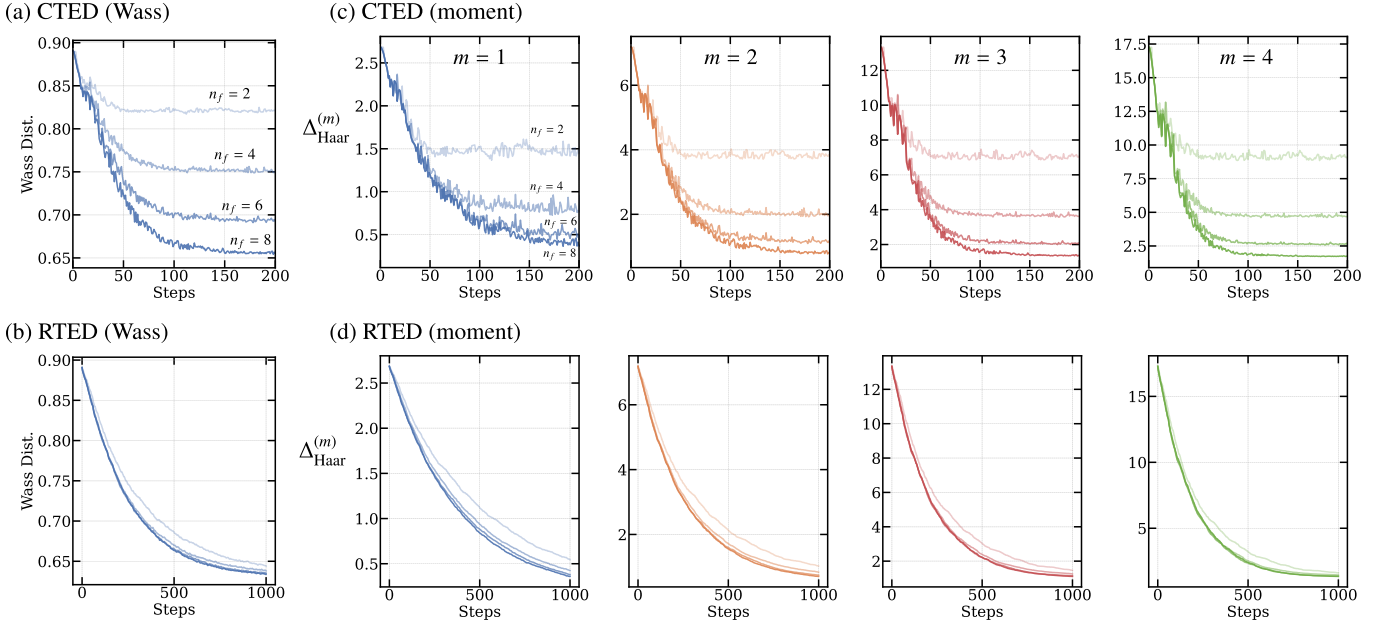


FIG. 3. 1-Wasserstein distance and normalized moment distance $\Delta_{\text{Haar}}^{(m)}(k)$ between the diffused ensemble and the Haar-random ensemble versus diffusion step k , for CTED and RTED. Results are shown for different complement sizes $n_f \in \{2, 4, 6, 8\}$ and moment orders m .

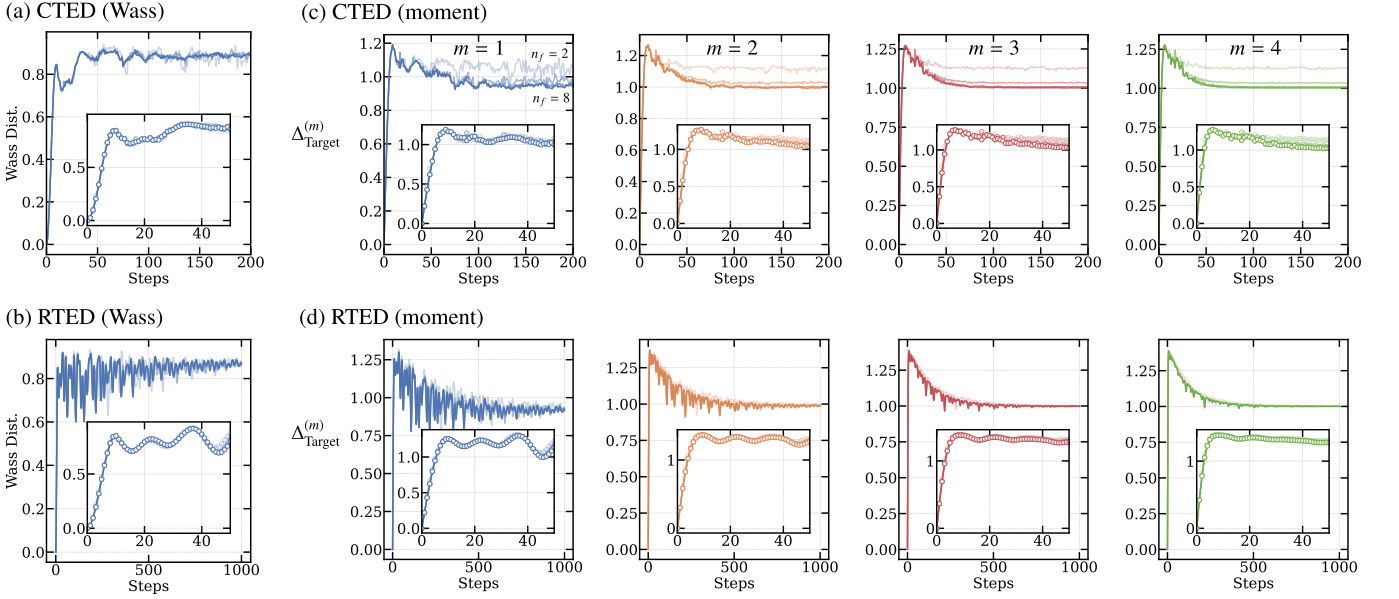


FIG. 4. 1-Wasserstein distance and normalized moment distance $\Delta_{\text{Haar}}^{(m)}(k)$ between the diffused ensemble and the target multi-cluster ensemble versus diffusion step k , for CTED and RTED. Results are shown for different complement sizes $n_f \in \{2, 4, 6, 8\}$ and moment orders m .

the classically-enhanced projected ensemble $\mathcal{E}^{(k)} = \{q(\mathbf{x}_j^{(k)})p_{\mathbf{x}}(\mathbf{z}_j^{(k)}; |\psi_{\mathbf{x}}(\mathbf{z}_j^{(k)})\rangle)\}_j$, we can define the m -th moment operator for this ensemble as

$$\rho_k^{(m)} = \sum_j q(\mathbf{x}_j^{(k)})p_{\mathbf{x}}(\mathbf{z}_j^{(k)}) \left(|\psi_{\mathbf{x}}(\mathbf{z}_j^{(k)})\rangle \langle \psi_{\mathbf{x}}(\mathbf{z}_j^{(k)})| \right)^{\otimes m}. \quad (6)$$

We compute the normalized Hilbert-Schmidt distance to

the m -th moment of the Haar ensemble and the target ensemble:

$$\Delta_{\text{Haar}}^{(m)}(k) = \frac{\|\rho_k^{(m)} - \rho_{\text{Haar}}^{(m)}\|_2}{\|\rho_{\text{Haar}}^{(m)}\|_2}, \quad (7)$$

$$\Delta_{\text{Target}}^{(m)}(k) = \frac{\|\rho_k^{(m)} - \rho_{\text{Target}}^{(m)}\|_2}{\|\rho_{\text{Target}}^{(m)}\|_2}. \quad (8)$$

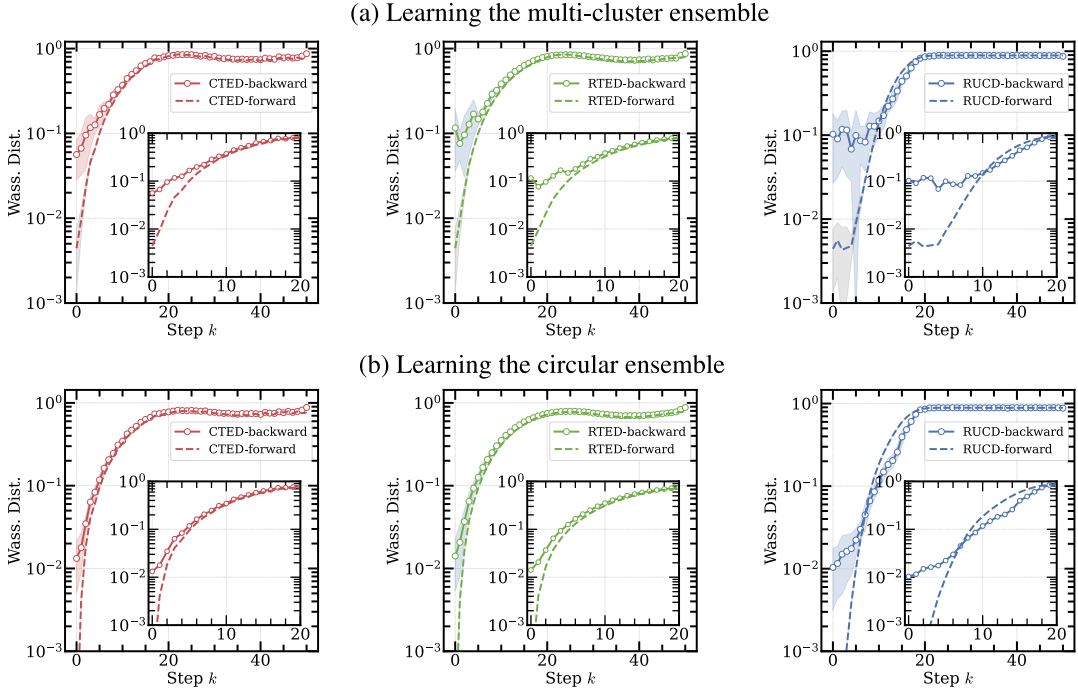


FIG. 5. 1-Wasserstein distances between the generated ensembles and the true ensemble over backward steps, sampled from (a) multi-cluster and (b) circular datasets of quantum states, for CTED (left), RTED (center), and RUCD (right). The backward process (solid lines with circle markers) is compared to the forward diffusion (dotted lines). Lines and shaded areas represent the mean and standard deviation over ten trials.

Figures 3 and 4 characterize the forward diffusion dynamics induced by chaotic time evolution, quantified by the 1-Wasserstein distance and the normalized moment distances. Figure 3 reports the distance between the diffused ensemble and the Haar-random ensemble for both CTED and RTED, while varying the number of diffusion steps and the complement-system size $n_f \in \{2, 4, 6, 8\}$. For CTED, all metrics exhibit a rapid initial decay followed by saturation at finite values that depend systematically on n_f and the moment order m . Increasing n_f lowers the saturation plateau, indicating that deviations from Haar randomness are dominated by finite-size effects associated with the complement system. Higher-order moments saturate at larger residual values, reflecting the persistence of non-Haar correlations at finer statistical resolution. RTED shows slower decay with increasing diffusion steps but continues to approach smaller distances at long times. This behavior arises because at the k -th diffusion step, RTED repeatedly applies the same short-time unitary evolution while coupling the main system to independently initialized complement subsystems. As a result, the effective environment size grows proportionally to kn_f , progressively suppressing finite-size effects. The results do not imply that the convergence to a Haar-random ensemble. Instead, both approach a universal finite-temperature ensemble consistent with chaotic dynamics and conserved quantities.

Figure 4 compares the diffused ensemble directly to the

target multi-cluster distribution. For both CTED and RTED, the distance to the target ensemble increases during the diffusion process and subsequently saturates at a finite value, indicating that the forward diffusion drives the ensemble away from the target distribution toward a stationary noisy ensemble. CTED exhibits smoother convergence, leading to more stable backward targets, whereas RTED shows larger temporal fluctuations due to repeated reinitialization of the complement system, while reaching comparable asymptotic distances.

We consider the backward process with $K = 50$ steps. Each denoising operation V_k is trained for 1000 epochs using 1000 samples with a mini-batch size of 100, minimizing the 1-Wasserstein distance. Figure 5 compares the backward generative performance of CTED, RTED, and RUCD using the 1-Wasserstein distance between the generated ensemble \mathcal{S}'_k and the true ensemble \mathcal{S}'_0 , for both multi-cluster and circular quantum datasets. In general, the final distances are comparable for all methods. Particularly, for CTED and RTED, the backward process closely mirrors the corresponding forward diffusion, exhibiting smooth and monotonic convergence with relatively small variance across trials. This indicates that the chaotic diffusion dynamics generate structured noise that can be effectively inverted by the backward process. In contrast, RUCD exhibits significantly larger fluctuations and a pronounced mismatch between forward and backward curves, particularly at early steps, reflecting

the difficulty of inverting near-Haar random diffusion.

Learning Quantum Chemistry Distribution

We apply our framework to the QM9 dataset [31], a standard benchmark in computational chemistry. QM9 comprises approximately 1.34×10^5 equilibrium geometries of small organic molecules containing up to nine heavy atoms (C, N, O, and F), along with additional hydrogen atoms, for a maximum of 29 atoms per molecule. Each entry includes molecular properties and three-dimensional structural information, making the dataset widely used for tasks such as molecular property prediction and 3D structure generation [5]. Due to the current limitations of our quantum simulations, processing the full dataset is not feasible. We therefore restrict our study to molecules with exactly eight heavy atoms and two distinct ring systems, resulting in a more structurally homogeneous subset of 4236 molecules. The 3D structures of these molecules are encoded into 7-qubit quantum states following the encoding scheme in Ref. [5].

In our numerical experiments, we set $n_m = 7$, $n_f = 3$, and use $K = 20$ diffusion steps. Each backward denoising unitary V_k is implemented by a hardware-efficient ansatz with $L = 10$ layers. We train each V_k for 1000 epochs using 2000 training samples with mini-batch size 100, minimizing the 1-Wasserstein distance. For this non-trivial distribution in a high-dimensional Hilbert space, however, accurate backward denoising can require deeper circuits and longer training, making direct learning in the full 7-qubit space challenging.

To mitigate this, we adopt a latent-space strategy [32] based on a quantum autoencoder (QAE) [33]. Specifically, we first train a QAE to compress the 7-qubit states into a $n_l = 4$ -qubit latent representation, and then perform diffusion and denoising in the latent space. The QAE encoder is implemented as a depth-20 hardware-efficient circuit consisting of single-qubit RY parameterized rotations followed by a ring of CNOT gates repeated across layers. It is trained to decouple the remaining “trash” qubits by maximizing their overlap with the $|0 \dots 0\rangle$ state. We optimize the QAE parameters using the Adam optimizer with a learning rate of 0.001 for 2000 epochs. After training, the decoder (implemented as the approximate inverse circuit) maps generated latent states back to the original 7-qubit space, enabling sampling in the full molecular state representation while reducing the learning burden of the diffusion model. In the latent space, we perform forward and backward diffusion with $n_m = 4$, $n_f = 2$ qubits and use $K = 20$ diffusion steps. Other training conditions are the same as training in the full 7-qubit space.

Figure 6 compares the performance of the backward diffusion (denoising) process when it is learned directly in the full Hilbert space (“Full”) and when it is learned in

the latent space obtained from a quantum autoencoder (“Latent”), followed by decoding back to the original space. For all three diffusion schemes (CTED, RTED, and RUCD), backward denoising learned in the latent space consistently achieves lower Wasserstein distances and reduced fluctuations compared to denoising learned directly in the full Hilbert space. This indicates that the backward maps trained in the latent representation are able to more accurately invert the diffusion process, particularly at intermediate and late backward steps where the input states are more strongly corrupted. The improvement is especially evident in the smoother growth of the Wasserstein distance and the smaller variance across trials, demonstrating enhanced stability and robustness of the learned denoising dynamics.

This behavior can be understood by viewing the quantum autoencoder as an information bottleneck that reshapes the inverse problem faced by the backward diffusion. By compressing the original 7-qubit molecular states into a lower-dimensional latent space, the autoencoder isolates the dominant degrees of freedom that characterize the data distribution while discarding directions that contribute weakly to reconstruction but strongly to noise amplification. As a result, the backward learned in the latent space operates on a reduced manifold where the inverse mapping from noisy states to cleaner ones is better conditioned. After decoding, the reconstructed full-space states therefore remain closer to the target ensemble than those obtained by backward denoising trained directly in the full Hilbert space.

Resource Comparison

To clarify the resource advantage of CTED and RTED, we compare its implementation cost with RUCD in terms of entangling-gate complexity and circuit depth. In our implementation with RUCD, each diffusion layer contains an all-to-all entangling block, which requires $O(n_m^2)$ two-qubit gates. Over K diffusion steps, the total entangling gate count scales as $O(Kn_m^2)$ per sample, leading to significant compilation and calibration overhead.

In contrast, CTED and RTED implement diffusion through continuous-time evolution under a fixed chaotic Hamiltonian. On analog platforms such as Rydberg arrays or trapped-ion systems, this Hamiltonian is realized via global, time-independent control fields. Each diffusion step therefore corresponds to physical time evolution rather than a compiled gate sequence, and the required control resources do not scale with n_m^2 in the same manner. The primary cost is total evolution time $T = K\Delta t$, rather than circuit depth.

This distinction becomes especially important on analog hardware, where global Hamiltonian evolution is native but synthesizing deep random circuits with all-to-all entangling gates is experimentally demanding. Hence,

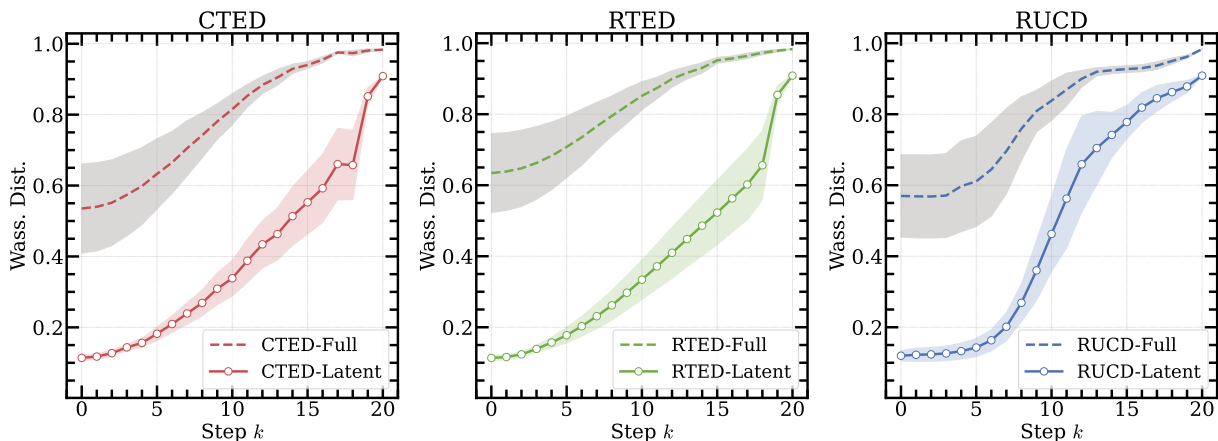


FIG. 6. 1-Wasserstein distance between the generated ensemble and the true ensemble of the QM9 subset dataset as a function of diffusion step k , comparing backward diffusion performed in the full Hilbert space (“Full”, dashed) and in the latent space learned by a quantum autoencoder (“Latent”, solid). Results are shown for CTED (left), RTED (center), and RUCD (right). Shaded regions denote the standard deviation over ten trials.

chaotic diffusion provides a hardware-efficient alternative to circuit-based scrambling while maintaining comparable generative performance

Noise Robustness

We investigate the robustness of CTED, RTED, and RUCD to an explicit stochastic noise and quantify the degradation in the 1-Wasserstein distance between the generated and target ensembles. We do not directly compare the RUCD and CTED/RTED noise models, because the dominant error mechanisms differ qualitatively. RUCD is primarily affected by gate and control errors accumulated per applied pulse, whereas CTED/RTED is primarily affected by decoherence accumulated continuously during analog Hamiltonian evolution and measurement. Accordingly, we perform within-method sensitivity analyses using noise models that reflect the most relevant physical mechanism for each setting.

For RUCD, we inject stochastic single-qubit Pauli errors after each single-qubit rotation gate. After every application of $e^{-i\theta Y/2}$ and $e^{-i\theta Z/2}$ in the scrambling circuit, we apply a random Pauli operator $P \in \{X, Y, Z\}$ with probability p_1 , chosen uniformly among the three Paulis. When no error occurs, the circuit proceeds ideally. This corresponds to a per-gate Pauli-depolarizing channel acting after the unitary U at each noisy gate location:

$$\mathcal{N}(\rho) = (1 - p_1)U\rho U^\dagger + \frac{p_1}{3} \sum_{P \in \{X, Y, Z\}} PU\rho U^\dagger P. \quad (9)$$

Since such errors accumulate with circuit depth, the effective corruption strength scales approximately with the number of single-qubit gate locations N_{1q} . For small p_1 ,

the expected number of injected Pauli errors approximates $p_1 N_{1q}$, and the overall deviation increases roughly linearly in p_1 at fixed depth.

In the CTED and RTED using the chaotic Hamiltonian scrambling module, we consider a standard pure dephasing model implemented at the state-vector trajectory level. After coherent evolution $U(t) = e^{-iHt}$, each qubit undergoes an independent stochastic Z flip with probability $p_\phi(t) = \frac{1 - e^{-\gamma_\phi t}}{2}$, which corresponds to an unraveling of phase-damping noise (the chaotic evolution is unitary when $\gamma_\phi = 0$). We define $p_2 = p_\phi(\Delta t)$ as the dephasing strength after one diffusion step duration in the RTED. Then $p_\phi(k\Delta t) = \frac{1 - (1 - 2p_2)^k}{2}$ is the noise probability applied after k th step in CTED. Note that p_1 (in RUCD) and p_2 (in CTED and RTED) are not directly comparable in hardware realism.

Figure 7 summarizes the noise sensitivity of CTED, RTED, and RUCD as the noise levels p_2 and p_1 increase for the task of learning the multi-cluster distribution of quantum data. Here, we consider the setting in which samples from the original (clean) target ensemble are not available during training; instead, the model is trained only on diffused samples, which serve as the noisy training data. CTED and RTED remain stable across the noise range, with Wasserstein distances staying bounded.

RUCD exhibits a much sharper breakdown. Beyond a moderate noise level, many instances rapidly jump to Wasserstein distances of order unity, indicating a failure to recover the target ensemble. This behavior is consistent with the structure of the injected noise. Because RUCD relies on explicit circuit-based scrambling composed of many single-qubit rotations, it contains a large number N_{1q} of noisy gate locations. At high p_1 , the accumulated corruption grows quickly with circuit depth,

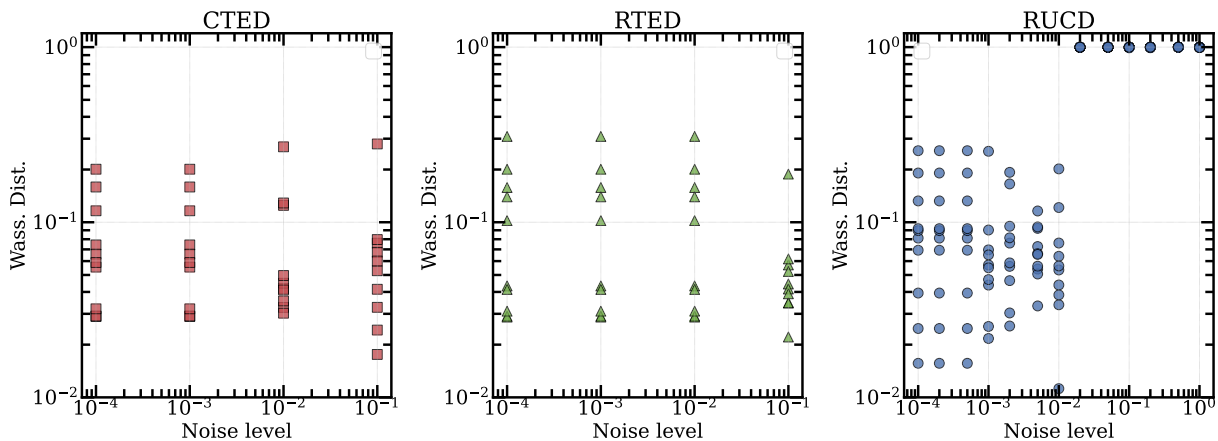


FIG. 7. Wasserstein distance between the generated ensemble and the target ensemble as a function of the noise level for CTED (left), RTED (center), and RUCD (right). Each marker corresponds to an independent run. CTED and RTED exhibit gradual degradation as noise increases, whereas RUCD shows a sharp loss of performance at higher noise levels.

effectively driving the diffused states toward highly randomized distributions at early forward steps. Consequently, the learned backward map is unable to recover the target, as the forward channel has already erased the necessary information.

Unlike the gate-based implementation of RUCD, where errors accumulate across many noisy operations, the analog execution of CTED and RTED involves fewer locations at which this noise model applies, resulting in less accumulated error. CTED and RTED generate the ensemble by measuring the complement system \mathcal{F} and retaining the post-measurement state on the main system \mathcal{M} . These measurements collapse and discard the complement subsystem, preventing errors in \mathcal{F} from coherently propagating across multiple steps. Note that CTED and RTED are still sensitive to time-integrated decoherence affecting \mathcal{M} during evolution.

We provide a mathematical explanation for the intrinsic robustness of CTED and RTED under coherent errors in the complement system \mathcal{F} . Each diffusion step in chaotic diffusion schemes consists of (i) coupling the main system \mathcal{M} to a complement \mathcal{F} via a joint Hamiltonian evolution, followed by (ii) a projective measurement on \mathcal{F} and discarding \mathcal{F} . This measure-and-discard structure has two stabilizing consequences. First, once \mathcal{F} is measured and discarded, any noise acting on \mathcal{F} cannot coherently propagate through \mathcal{F} across diffusion steps (especially in RTED where \mathcal{F} is re-prepared at each step). Second, errors on \mathcal{F} immediately before measurement effectively modify the measurement rule on \mathcal{F} rather than inducing a coherent, accumulating miscalibration on \mathcal{M} . We formalize this observation by showing that arbitrary noise on \mathcal{F} prior to the measurement is equivalent to measuring \mathcal{F} with a noisy POVM, and that Pauli noise on measured qubits leads only to outcome relabeling, leaving permutation-invariant ensemble statistics unchanged.

Lemma 1 (Noise becomes POVM). *Let $\mathcal{N}_{\mathcal{F}}$ be an arbitrary CPTP noise channel acting on \mathcal{F} immediately before the measurement. Then the measurement statistics under $\mathcal{N}_{\mathcal{F}}$ are identical to those obtained by measuring the noiseless state $|\Phi\rangle$ with a POVM $\{E_z\}_z$ on \mathcal{F} defined by*

$$E_z := \mathcal{N}_{\mathcal{F}}^{\dagger}(|z\rangle\langle z|), \quad E_z \succeq 0, \quad \sum_z E_z = \mathbb{I}_{\mathcal{F}}, \quad (10)$$

where $\mathcal{N}_{\mathcal{F}}^{\dagger}$ is the adjoint (Heisenberg-picture) map. In particular, the noisy outcome probability is

$$\tilde{p}(z) = \langle \Phi | (\mathbb{I}_{\mathcal{M}} \otimes E_z) | \Phi \rangle. \quad (11)$$

Proof. Let $\rho = |\Phi\rangle\langle\Phi|$. Applying $\mathcal{N}_{\mathcal{F}}$ on \mathcal{F} gives $\tilde{\rho} = (\mathbb{I}_{\mathcal{M}} \otimes \mathcal{N}_{\mathcal{F}})(\rho)$. The noisy probability of measuring z is

$$\tilde{p}(z) = \text{Tr}[(\mathbb{I}_{\mathcal{M}} \otimes |z\rangle\langle z|) \tilde{\rho}] = \text{Tr}\left[(\mathbb{I}_{\mathcal{M}} \otimes \mathcal{N}_{\mathcal{F}}^{\dagger}(|z\rangle\langle z|)) \rho\right], \quad (12)$$

which yields Eq. (11) with E_z defined in Eq. (10). Positivity and completeness follow from complete positivity and trace preservation of $\mathcal{N}_{\mathcal{F}}$. \square

Lemma 1 formalizes the classicalization mechanism: any noise on the measured subsystem can be absorbed into the measurement rule (a noisy POVM), rather than coherently accumulating on \mathcal{M} as an unknown unitary distortion.

We next specialize to Pauli errors acting on measured qubits in \mathcal{F} immediately before a computational-basis measurement. Let $q \in \mathcal{F}$ denote a measured qubit and e_q the bitstring with a 1 at position q and 0 elsewhere.

Corollary 1 (Pauli relabeling invariance). *Consider a projected-ensemble step in which \mathcal{F} is measured in the computational basis. If, immediately before measurement, a Pauli operator $P_q \in \{X_q, Y_q, Z_q\}$ acts on a measured qubit $q \in \mathcal{F}$, then: (i) Z_q leaves the conditional (un-normalized) post-measurement state on \mathcal{M} unchanged up*

to a global phase and hence does not change the projected ensemble; (ii) X_q and Y_q permute (relabel) the measurement outcome as $\mathbf{z} \mapsto \mathbf{z} \oplus \mathbf{e}_q$ (up to a phase for Y_q), leaving the set of conditional states invariant up to relabeling. Consequently, any permutation-invariant ensemble functional is unchanged, including the moment operators.

Proof. Let $|\Phi\rangle$ be the joint pre-measurement state on $\mathcal{M} + \mathcal{F}$ and define $|\tilde{\Phi}_{\mathcal{M}}(\mathbf{z})\rangle = (\mathbb{I}_{\mathcal{M}} \otimes \langle \mathbf{z} |) |\Phi\rangle$. If Z_q acts before measurement, then $Z_q |\mathbf{z}\rangle = (-1)^{z_q} |\mathbf{z}\rangle$, where z_q is the bit value of the qubit q . Hence, $|\tilde{\Phi}_{\mathcal{M}}^{(Z_q)}(\mathbf{z})\rangle = (\mathbb{I}_{\mathcal{M}} \otimes \langle \mathbf{z} |) (\mathbb{I}_{\mathcal{M}} \otimes Z_q) |\Phi\rangle = (-1)^{z_q} |\tilde{\Phi}_{\mathcal{M}}(\mathbf{z})\rangle$, which changes only a global phase and therefore leaves both $p(\mathbf{z}) = \|\tilde{\Phi}_{\mathcal{M}}(\mathbf{z})\|^2$ and the normalized conditional state $|\Phi_{\mathcal{M}}(\mathbf{z})\rangle$ unchanged.

If X_q acts before measurement, then $X_q |\mathbf{z}\rangle = |\mathbf{z} \oplus \mathbf{e}_q\rangle$, giving $|\tilde{\Phi}_{\mathcal{M}}^{(X_q)}(\mathbf{z})\rangle = (\mathbb{I}_{\mathcal{M}} \otimes \langle \mathbf{z} |) (\mathbb{I}_{\mathcal{M}} \otimes X_q) |\Phi\rangle = (\mathbb{I}_{\mathcal{M}} \otimes \langle \mathbf{z} \oplus \mathbf{e}_q |) |\Phi\rangle = |\tilde{\Phi}_{\mathcal{M}}(\mathbf{z} \oplus \mathbf{e}_q)\rangle$, so the conditional outputs are permuted by $\mathbf{z} \mapsto \mathbf{z} \oplus \mathbf{e}_q$. For $Y_q = iX_q Z_q$, the same permutation holds up to an outcome-dependent phase, which again does not affect $p(\mathbf{z})$ or the normalized conditional state. Finally, moment operators and other permutation-invariant ensemble statistics are unchanged under relabeling of outcomes, since the sums over outcomes are invariant under bijections of the index set. This completes the proof. \square

SUMMARY AND DISCUSSION

We have proposed a quantum diffusion model with two schemes, CTED and RTED, using chaotic Hamiltonian evolution. These schemes match RUCD’s accuracy in learning quantum data distributions while eliminating its complex spatio-temporal control, making them ideal for analog quantum systems. Our experiments on synthetic multi-cluster and circular datasets demonstrate that CTED and RTED achieve generative accuracy comparable to RUCD. In the QM9 molecular dataset, we further show that combining chaotic diffusion with a quantum autoencoder enables stable learning in a compressed latent space, significantly improving performance in high-dimensional Hilbert spaces.

Our chaotic diffusion processes are designed to be compatible with analog quantum simulators where dynamics is generated by a time-independent many-body Hamiltonian with minimal spatiotemporal control. In our simulations, we used a mixed-field Ising model on a 1D chain, where the competition between interactions and non-commuting fields places the system in a chaotic (thermalizing) regime away from integrable limits. This structure maps naturally to several leading platforms. In Rydberg atom arrays, effective Ising couplings arise from blockade-induced interactions, while a global Rabi drive and detuning implement the transverse (X) and longitudinal (Z) fields [34]. Site-resolved mea-

surement enables direct implementation of the complement measurement required in projected ensemble, and local re-initialization can support RTED-style repeated short evolutions. In trapped-ion simulators, phonon-mediated interactions generate programmable long-range $Z_i Z_j$ coupling with tunable range, and global drives implement transverse fields [35]. The complement measurement and reset is feasible within typical experimental workflows. Cold-atom implementations are most direct in Rydberg-dressed lattice settings (similar to Rydberg arrays), while superexchange-based lattice spin models may require additional engineering to realize the mixed-field Ising form [36].

Connectivity and boundary conditions mainly affect the mixing time and the stationary projected ensemble itself, since our endpoint is generally not Haar at finite energy density. This yields a platform-specific schedule that fixes the effective diffusion strength while allowing the underlying connectivity to vary.

Because chaoticity can be imperfect in realistic devices, it is important to understand sensitivity to near-integrable regimes. Our framework does not require maximal scrambling. Rather, it requires that the forward channel sufficiently “forget” detailed input information while remaining learnable by the backward model. In practice, this can be assessed by sweeping Hamiltonian parameters and monitoring simple forward indicators such as purity decay or local observable relaxation alongside backward-model stability and sample quality. We expect degradation primarily when dynamics approaches integrable limits, where mixing slows and the projected ensemble becomes strongly structured. Away from these limits, the method should remain robust under realistic connectivity and moderate Hamiltonian imperfections.

Beyond hardware efficiency, chaotic diffusion modifies the structure of the forward process. RUCD is designed to approximate Haar-random ensembles at large diffusion steps, whereas CTED and RTED converge to finite-temperature projected ensembles constrained by conserved quantities. In our numerical experiments, this difference manifests in smoother forward trajectories and reduced fluctuations during backward training for CTED and RTED compared to RUCD. While all three approaches achieve comparable final generative accuracy in the regimes studied, the chaotic diffusion schemes avoid full Haar over-scrambling and may provide a better-conditioned inverse problem in certain parameter regimes. However, for a fair comparison between these methods, it requires a scrambling schedule to match the scrambling scale between protocols. For example, we can match the scrambling level by calibrating each forward process to the same scalar corruption scale. A systematic theoretical analysis of this potential advantage remains an important direction for future work.

-
- * tran.quochoan@fujitsu.com
- [1] S. Lloyd and C. Weedbrook, Quantum generative adversarial learning, *Phys. Rev. Lett.* **121**, 040502 (2018).
 - [2] C. Zoufal, A. Lucchi, and S. Woerner, Quantum generative adversarial networks for learning and loading random distributions, *npj Quantum Information* **5**, 10.1038/s41534-019-0223-2 (2019).
 - [3] H.-L. Huang, Y. Du, M. Gong, Y. Zhao, Y. Wu, C. Wang, S. Li, F. Liang, J. Lin, Y. Xu, R. Yang, T. Liu, M.-H. Hsieh, H. Deng, H. Rong, C.-Z. Peng, C.-Y. Lu, Y.-A. Chen, D. Tao, X. Zhu, and J.-W. Pan, Experimental quantum generative adversarial networks for image generation, *Phys. Rev. Appl.* **16**, 024051 (2021).
 - [4] A. Khoshaman, W. Vinci, B. Denis, E. Andriyash, H. Sadeghi, and M. H. Amin, Quantum variational autoencoder, *Quantum Science and Technology* **4**, 014001 (2018).
 - [5] H. Wu, X. Ye, and J. Yan, QVAE-mole: The quantum VAE with spherical latent variable learning for 3-d molecule generation, in *Advances in Neural Information Processing Systems 38 (NeurIPS)* (2024).
 - [6] M. L. Wall, M. R. Abernathy, and G. Quiroz, Generative machine learning with tensor networks: Benchmarks on near-term quantum computers, *Phys. Rev. Res.* **3**, 023010 (2021).
 - [7] A. Cacioppo, L. Colantonio, S. Bordoni, and S. Giagu, *Quantum diffusion models* (2023), [arXiv:2311.15444](https://arxiv.org/abs/2311.15444).
 - [8] M. Parigi, S. Martina, and F. Caruso, Quantum-noise-driven generative diffusion models, *Advanced Quantum Technologies* , 2300401 (2024).
 - [9] Editorial, Seeking a quantum advantage for machine learning, *Nat. Mach. Intell.* **5**, 813–813 (2023).
 - [10] M. Y. Niu, A. Zlokapa, M. Broughton, S. Boixo, M. Mohseni, V. Smelyanskiy, and H. Neven, Entangling quantum generative adversarial networks, *Phys. Rev. Lett.* **128**, 220505 (2022).
 - [11] L. Kim, S. Lloyd, and M. Marvian, Hamiltonian quantum generative adversarial networks, *Phys. Rev. Res.* **6**, 033019 (2024).
 - [12] Q. H. Tran, S. Kikuchi, and H. Oshima, Variational denoising for variational quantum eigensolver, *Phys. Rev. Res.* **6**, 023181 (2024).
 - [13] K. Beer and G. Müller, *Dissipative quantum generative adversarial networks* (2021), [arXiv:2112.06088](https://arxiv.org/abs/2112.06088).
 - [14] J. R. McClean, S. Boixo, V. N. Smelyanskiy, R. Babbush, and H. Neven, Barren plateaus in quantum neural network training landscapes, *Nat. Commun.* **9**, 4812 (2018).
 - [15] B. Zhang, P. Xu, X. Chen, and Q. Zhuang, Generative quantum machine learning via denoising diffusion probabilistic models, *Phys. Rev. Lett.* **132**, 100602 (2024).
 - [16] T. Schuster, J. Haferkamp, and H.-Y. Huang, Random unitaries in extremely low depth, *Science* **389**, 92 (2025).
 - [17] H.-Y. Huang, R. Kueng, and J. Preskill, Predicting many properties of a quantum system from very few measurements, *Nat. Phys.* **16**, 1050 (2020).
 - [18] K. Chinzei, Q. H. Tran, N. Matsumoto, Y. Endo, and H. Oshima, *Learning quantum many-body data locally: A provably scalable framework* (2025), [arXiv:2509.13705](https://arxiv.org/abs/2509.13705).
 - [19] J. Choi, A. L. Shaw, I. S. Madjarov, X. Xie, R. Finkelstein, J. P. Covey, J. S. Cotler, D. K. Mark, H.-Y. Huang, A. Kale, H. Pichler, F. G. S. L. Brandão, S. Choi, and M. Endres, Preparing random states and benchmarking with many-body quantum chaos, *Nature* **613**, 468 (2023).
 - [20] J. S. Cotler, D. K. Mark, H.-Y. Huang, F. Hernández, J. Choi, A. L. Shaw, M. Endres, and S. Choi, Emergent quantum state designs from individual many-body wave functions, *PRX Quantum* **4**, 010311 (2023).
 - [21] W.-K. Mok, T. Haug, A. L. Shaw, M. Endres, and J. Preskill, Optimal conversion from classical to quantum randomness via quantum chaos, *Phys. Rev. Lett.* **134**, 180403 (2025).
 - [22] N. D. Varikuti and S. Bandyopadhyay, Unraveling the emergence of quantum state designs in systems with symmetry, *Quantum* **8**, 1456 (2024).
 - [23] M. McGinley and T. Schuster, *The scrooge ensemble in many-body quantum systems* (2025), [arXiv:2511.17172](https://arxiv.org/abs/2511.17172).
 - [24] S. Manna, S. Roy, and G. J. Sreejith, Projected ensemble in a system with locally supported conserved charges, *Phys. Rev. B* **111**, 144302 (2025).
 - [25] W.-K. Mok, T. Haug, W. W. Ho, and J. Preskill, *Nature is stingy: Universality of scrooge ensembles in quantum many-body systems* (2026), [arXiv:2601.00266](https://arxiv.org/abs/2601.00266).
 - [26] S.-X. Zhang, J. Allcock, Z.-Q. Wan, S. Liu, J. Sun, H. Yu, X.-H. Yang, J. Qiu, Z. Ye, Y.-Q. Chen, C.-K. Lee, Y.-C. Zheng, S.-K. Jian, H. Yao, C.-Y. Hsieh, and S. Zhang, TensorCircuit: a Quantum Software Framework for the NISQ Era, *Quantum* **7**, 912 (2023).
 - [27] J. Bradbury, R. Frostig, P. Hawkins, M. J. Johnson, C. Leary, D. Maclaurin, G. Necula, A. Paszke, J. VanderPlas, S. Wanderman-Milne, and Q. Zhang, *JAX: composable transformations of Python+NumPy programs* (2018).
 - [28] Q. H. Tran, K. Chinzei, Y. Endo, and H. Oshima, *Source code of the paper “Learning quantum data distribution via chaotic quantum diffusion model”* (2026).
 - [29] M. Srednicki, Chaos and quantum thermalization, *Phys. Rev. E* **50**, 888 (1994).
 - [30] L. D’Alessio, Y. Kafri, A. Polkovnikov, and M. Rigol, From quantum chaos and eigenstate thermalization to statistical mechanics and thermodynamics, *Advances in Physics* **65**, 239 (2016).
 - [31] R. Ramakrishnan, P. O. Dral, M. Rupp, and O. A. von Lilienfeld, Quantum chemistry structures and properties of 134 kilo molecules, *Scientific Data* **1**, 10.1038/sdata.2014.22 (2014).
 - [32] N. Raj, R. Sangle, A. Singh, and K. K. Sabapathy, *Quantum generative adversarial autoencoders: Learning latent representations for quantum data generation* (2025), [arXiv:2509.16186](https://arxiv.org/abs/2509.16186).
 - [33] J. Romero, J. P. Olson, and A. Aspuru-Guzik, Quantum autoencoders for efficient compression of quantum data, *Quantum Science and Technology* **2**, 045001 (2017).
 - [34] H. Bernien, S. Schwartz, A. Keesling, H. Levine, A. Omran, H. Pichler, S. Choi, A. S. Zibrov, M. Endres, M. Greiner, V. Vuletić, and M. D. Lukin, Probing many-body dynamics on a 51-atom quantum simulator, *Nature* **551**, 579–584 (2017).
 - [35] J. W. Britton, B. C. Sawyer, A. C. Keith, C.-C. J. Wang, J. K. Freericks, H. Uys, M. J. Biercuk, and J. J. Bollinger, Engineered two-dimensional ising interactions in a trapped-ion quantum simulator with hundreds of spins, *Nature* **484**, 489–492 (2012).
 - [36] C. Gross and I. Bloch, Quantum simulations with ultracold atoms in optical lattices, *Science* **357**, 995–1001 (2017).